An open source pipeline for design of experiments for hyperelastic models of the skin with applications to keloids

Danas Sutula, Aflah Elouneg, Marco Sensale, Franz Chouly, Jérôme Chambert, Arnaud Lejeune, Davide Baroli, Paul Hauseux, Stéphane P.A. Bordas, Emmanuelle Jacquet

To cite this version:

Danas Sutula, Aflah Elouneg, Marco Sensale, Franz Chouly, Jérôme Chambert, et al.. An open source pipeline for design of experiments for hyperelastic models of the skin with applications to keloids. Journal of the mechanical behavior of biomedical materials, 2020, 112, pp.103999. 10.1016/j.jmbbm.2020.103999 . hal-03036303

HAL Id: hal-03036303
https://hal.science/hal-03036303v1

Submitted on 14 Jun 2024

An open source pipeline for design of experiments for hyperelastic models of the skin with applications to keloids

D. Sutula[a], A. Elouneg[a], M. Sensale[a,b], F. Chouly[c], J. Chambert[a], A. Lejeune[a], D. Baroli[d], P. Hauseux[b], S. Bordas[b,**], E. Jacquet[a,*]

[a] *Univ. Bourgogne Franche-Comté, FEMTO-ST Institute, Department of Applied Mechanics, Besançon, France.*
[b] *University of Luxembourg, Institute of Computational Engineering, Luxembourg. Department of Computer Science and Information Engineering, Asia University, Taichung, Taiwan. Department of Medical Research, China Medical University Hospital, China Medical University, Taichung, Taiwan.*
[c] *Univ. Bourgogne Franche-Comté, Institut de Mathématiques de Bourgogne, Dijon, France.*
[d] *RWTH, AICES, Aachen, Germany*

Abstract

The aim of this work is to characterize the mechanical parameters governing the in-plane behavior of human skin and, in particular, of a keloid-scar. We consider 2D hyperelastic bi-material model of a keloid and the surrounding healthy skin. The problem of finding the optimal model parameters that minimize the misfit between the model observations and the *in vivo* experimental measurements is solved using our in-house developed inverse solver that is based on the FEniCS finite element computational platform. The paper focuses on the model parameter sensitivity quantification with respect to the experimental measurements, such as the displacement field and reaction force measurements. The developed tools quantify the significance of different measurements on different model parameters and, in turn, give insight into a given model's ability to capture experimental measurements. Finally, an *a priori* estimate for the model parameter sensitivity is proposed that is independent of the actual measurements and that is defined in the

---

[*] Corresponding author : emmanuelle.jacquet@univ-fcomte.fr
[**] Corresponding author : stephane.bordas@alum.northwestern.edu

whole computational domain. This estimate is primarily useful for the design of experiments, specifically, in localizing the optimal displacement field measurement sites for the maximum impact on model parameter inference.

Key words: soft tissue, inverse problem, optimization, model sensitivity, FEniCS.

---

1. Introduction

Biomechanical modelling can provide valuable insight into the response of biological systems to mechanical loading (Hatze, 1974). The study of biomechanics ranges from the inner workings of cells (Niklas, 1992) to the mechanical properties of bones (Cowin, 2001) and soft tissues (Fung, 1993), and to the development and movement of limbs. In the context of human living tissues, the attention over the past few decades has been mainly on the biomechanical characterization of such biological materials as brain tissues (Van Dommelen et al., 2010; Rashid et al., 2014), tendons (Screen, 2008), meniscal tissue (Barrera et al., 2018), and skin (*in vivo*, *in vitro* and *ex vivo*) (Maiti et al., 2016; Annaidh et al., 2012; Ottenio et al., 2015; Pan et al., 2019).

In this paper, we focus on the patient-specific biomechanical characterization of human skin and, in particular, a keloid scar (Abdel-Fattah, 1976; Robles and Berg, 2007). Keloids are non-cancerous tumors that grow continuously on the skin for several reasons. The evolution of keloids is related to genetic (Halim et al., 2012), biological (Kim et al., 2000), and biomechanical factors (Ogawa, 2008; Ogawa et al., 2012). In this work we care about the latter kind of influence; for example, the state of stress inside a keloid and in the surrounding skin is known to play a significant role in the growth of a keloid (Akaishi et al., 2008; Ogawa et al., 2012; Nagasao et al., 2013). However, in order to be able to characterize the mechanical behavior of a skin-keloid tissue it is first necessary to identify a suitable material model and to determine the patient-specific model parameters. The model parameter inference is centered around the idea of minimizing the error between the model observations and the experimental measurements (Meijer et al., 1999). There are many phenomenological hyperelastic models that are designed to capture various non-linear behaviors of the skin undergoing large deformations (Evans and Holt, 2009; Wex et al., 2015; Bahreman et al., 2015). We cite for instance such models as Mooney-Rivlin (1948), Ogden (1972), Yeoh (1993) or the simplest one, the Neo-Hookean model (Pence and Gou, 2015).

Time-dependence, such as a time-varying Poisson's ratio, can be modeled by using a fractional viscoelastic constitutive model (Alotta et al., 2017, 2018).

There are many types of experiments for measuring the mechanical response of skin under static or even dynamic loading. The most common type of test is the uniaxial traction test (Wan Abas and Barbenel, 1982; Finlay, 1970; Meijer et al., 1999; Boyer et al., 2013). A biaxial test can be performed for characterizing anisotropic material behavior (Wan Abas, 1994). For small and curved regions other types of tests may be more appropriate such as suction (Müller et al., 2018; Laiacona et al., 2019), bulge (Tonge et al., 2013) or indentation (Pailler-Mattei et al., 2008) tests. Other non-invasive tests for measuring the dynamic response of skin include using ultrasound (Diridollou et al., 1998; Zhang and Greenleaf, 2007), ballistometry (Fthenakis et al., 1991) and other dynamic mechanisms (Finlay, 1970).

In this work, we rely on *in vivo* uniaxial extension experiments and apply an inverse modeling approach to infer the material model parameters for a supposed material model. We consider 2D models for the in-plane behavior of the skin assuming the Neo-Hookean type of material. The first model assumes just the healthy skin (without the keloid) whereas the second model considers the bi-material of healthy skin and a keloid. Subsequently, the sensitivity of the inferred model parameters is assessed with respect to the measurements such as the displacement field and reaction force measurements. In summary, this paper makes the following contributions.

1. Introduction of a numerical process based on an open-source framework to identify the mechanical parameters of a heterogeneous soft tissue.
2. Model parameter sensitivity quantification with respect to displacement field and reaction force measurements. The sensitivities reveal how significant the different measurements are on different model parameters. They can also be used in troubleshooting a given model, such as discovering why certain errors may be large between the model observations and experimental measurements.
3. A prior estimate of the model parameter sensitivities with respect to the displacement field measurements. The estimate is defined in the whole computational domain and it is independent of the actual displacement field measurements. The estimate is useful primarily in that it reveals the most important displacements measurement sites, which can be leveraged in the design of experiments.

2. Problem statement

2.1. In vivo experiments

The *in vivo* experiments are carried out using a custom-made extensometer (Jacquet et al., 2017a,b), as shown in Fig. 1b. The small device is fixed on a region of interest, such as around a keloid scar Fig. 1a, and a displacement-controlled uni-axial displacement test is performed. The reaction force is measured by a strain gauge whereas the surface displacement field is captured using 2D digital image correlation (DIC) (Avril et al., 2008; Boyer et al., 2013). A series of measurements of the reaction force and of the corresponding displacement field are obtained.[1] As the pad displacements are measured with a sufficiently high accuracy – it is reported in (Jacquet et al., 2017b) that the extensometer is equipped with a linear variable displacement transducer whose positional accuracy is approximately 38 (μm) – the pad displacement measurements are introduced directly as Dirichlet boundary conditions in the hyperelastic problem. Unfortunately, we were unable to quantify the errors in the displacement field measurements obtained via the DIC analysis including any errors due to the out of plane motion, which is unavoidable in practice (Sutton et al., 2008). We did, however, identify a small number of spurious displacements that we subsequently eliminated from consideration.

2.2. Hyperelastic problem

Consider a domain $\Omega \in \mathbb{R}^2$ of a hyperelastic medium. The domain boundary $\partial\Omega$ is composed of the Dirichlet boundary Ω_D (where displacements are known) and the Neumann boundary Ω_N (where tractions are known) such that $\partial\Omega = \partial\Omega_D \cup \partial\Omega_N$ and $\partial\ \Omega_D\ \cap\ \partial\ \Omega_N = \emptyset$. Considering a pure displacement load $\mathbf{u}_D$ prescribed on $\partial\Omega_D$, the potential energy of the hyperelastic solid consists of just the strain energy of deformation that reads

$$W(\mathbf{u}, \mathbf{m}) = \int_\Omega \psi(\mathbf{u}, \mathbf{m})\ \mathrm{d}x, \tag{1}$$

where $\mathbf{u}$ is the displacement field, $\psi(\mathbf{u}, \mathbf{m})$ is the strain energy density of a chosen material model and $\mathbf{m}$ are the model's parameters. The variational

---

[1] The present work uses experimental data that was previously published in Chambert et al. (2019).

(a) Keloid scar located on the left-upper arm ($X = 15\ mm$, $Y = 47\ mm$).

(b) Extensometer. The speckle pattern is used for capturing the displacements.

Figure 1: Experimental investigation into the mechanical response of human skin (Chambert et al., 2019).

(or weak) form of static equilibrium is obtained by differentiating $W(\mathbf{u}, \mathbf{m})$ with respect to $\mathbf{u}$ and requiring all the admissible variations to vanish:

$$F(\mathbf{u}, \mathbf{m}; \mathbf{v}) = \partial_{\mathbf{u}} W(\mathbf{u}, \mathbf{m})[\mathbf{v}] = 0 \quad \forall \mathbf{v} \in \mathcal{V}_0, \tag{2}$$

where $\partial_{\mathbf{u}}(\cdot)[\mathbf{v}]$ denotes a partial derivative with respect to the argument $\mathbf{u} \in \mathcal{V}$ in the direction of $\mathbf{v} \in \mathcal{V}_0$. Here, $\mathcal{V}$ and $\mathcal{V}_0$ are suitably chosen function spaces such that the weak form (2) is well defined, $\mathbf{u} \in \mathcal{V}$ satisfies the Dirichlet boundary conditions and $\mathbf{v} \in \mathcal{V}_0$ vanishes on the Dirichlet boundary.

2.3. Inverse problem

The cost functional for the surface displacement field misfit is defined as the sum of the local costs over the measurement steps $k = 1, \dots, N_{\mathrm{msr}}$

$$\mathfrak{J}_u = \sum_{k=1}^{N_{\mathrm{msr}}} \mathfrak{J}_u^{(k)} = \sum_{k=1}^{N_{\mathrm{msr}}} \mathfrak{J}_u^{(k)} \left(\mathbf{u}^{(k)}(\mathbf{m}), \mathbf{u}_{\mathrm{msr}}^{(k)} \right) = \sum_{k=1}^{N_{\mathrm{msr}}} \frac{1}{2} \int_{\Gamma_u} \left(\mathbf{u}^{(k)}(\mathbf{m}) - \mathbf{u}_{\mathrm{msr}}^{(k)} \right)^2 \, \mathrm{d}x, \tag{3}$$

where $\mathbf{u}^{(k)}(\mathbf{m})$ is the model displacement field under the boundary conditions of step k, $\mathbf{u}_{\mathrm{msr}}^{(k)}$ is the measured (experimentally obtained) displacement field, and Γ_u is the displacement field measurement surface.

The functional (3) is generally insufficient to capture all the information needed to infer all the model parameters. In particular, the model parameters that carry units of pressure (N/mm^2) can not be determined without measurements of a related quantity. Therefore, an additional cost functional is introduced that is a measure of the pad reaction force misfit

$$\mathfrak{J}_f = \sum_{k=1}^{N_{\text{msr}}} \mathfrak{J}_f^{(k)} = \sum_{k=1}^{N_{\text{msr}}} \mathfrak{J}_f^{(k)} \left(f^{(k)}(\mathbf{m}), f_{\text{msr}}^{(k)} \right) = \sum_{k=1}^{N_{\text{msr}}} \frac{1}{2} \left(f^{(k)}(\mathbf{m}) - f_{\text{msr}}^{(k)} \right)^2 \tag{4}$$

The model reaction force $f^{(k)}$ is obtained by integrating the pad traction $\mathbf{T}$ on the pad surface Γ_f

$$f^{(k)}(\mathbf{m}) = f\left(\mathbf{u}^{(k)}(\mathbf{m}), \mathbf{m}\right) = \int_{\Gamma_f} \mathbf{T}\left(\mathbf{u}^{(k)}(\mathbf{m}), \mathbf{m}\right) \cdot \mathbf{N}_{\text{pad}} \, \mathrm{d}s, \tag{5}$$

where $\mathbf{N}_{\text{pad}}$ is the pad displacement direction and $f_{\text{msr}}^{(k)}(\mathbf{m})$ is the experimentally measured reaction force. Finally, the displacement and the reaction force misfit costs can be combined in a weighted average sense to obtain the total cost of the model

$$\mathfrak{J}(\mathbf{m}) = \mathfrak{J}_u(\mathbf{m}) + w\,\mathfrak{J}_f(\mathbf{m}) \tag{6}$$

where $w > 0$ is the weight that also serves to rescale $\mathfrak{J}_f$ (since its units are different from of $\mathfrak{J}_u$).[2]

The inverse problem may be stated as follows. Find the model parameters $\mathbf{m}^\star$ such that the cost $\mathfrak{J}(\mathbf{m})$ is minimized (or stationary) with respect to $\mathbf{m}$ and the weak form of static equilibrium $F(\mathbf{u}^{(k)}, \mathbf{m}; \mathbf{v}) = 0$ is satisfied at each step $k = 1, 2, \ldots, N_{\text{msr}}$. In summary, the inverse problem reads

$$\mathbf{m}^\star = \arg\left(D_{\mathbf{m}}\mathfrak{J}(\mathbf{m}) = 0\right) \tag{7}$$

$$\text{subject to: } F(\mathbf{u}^{(k)}, \mathbf{m}; \mathbf{v}) = 0$$

$$\forall \mathbf{v} \in \mathcal{V}_0,\ k = 1, 2, \ldots, N_{\text{msr}} \tag{8}$$

where $D_{\mathbf{m}}\mathfrak{J}$ is the total derivative of $\mathfrak{J}(\mathbf{m})$ with respect to $\mathbf{m}$.

---

[2] In our specific test cases, the choice of w was not found to be very important because the costs $\mathfrak{J}_u$ and $\mathfrak{J}_f$ happened to affect different model parameters. As such, w acted more like a stabilization than a weight.

3. Solution method

The total derivative of $\mathfrak{J}(\mathbf{m})$ with respect to $\mathbf{m}$ is expressed as

$$D_{\mathbf{m}}\mathfrak{J} = \sum_{k=1}^{N_{\mathrm{msr}}} \partial_{\mathbf{m}}\mathfrak{J}^{(k)} + [D_{\mathbf{m}}\mathbf{u}^{(k)}]^T \partial_{\mathbf{u}}\mathfrak{J}^{(k)} \tag{9}$$

The derivative $D_{\mathbf{m}}\mathbf{u}^{(k)}$ can be computed by considering the weak form of static equilibrium (2). Firstly, suppose the current solution state ($\mathbf{u}^{(k)}$, $\mathbf{m}$) satisfies (2). Now consider an arbitrary perturbation $\delta\mathbf{m}$ and the new solution state ($\mathbf{u}^{(k)} + \delta\mathbf{u}$, $\mathbf{m} + \delta\mathbf{m}$), where $\delta\mathbf{u} = D_{\mathbf{m}}\mathbf{u}^{(k)}[\delta\mathbf{m}]$. We can find $D_{\mathbf{m}}\mathbf{u}^{(k)}$ such that the new state satisfies (2) for any admissible $\delta\mathbf{m}$ as follows

$$F(\mathbf{u}^{(k)}, \mathbf{m}; \mathbf{v}) = F(\mathbf{u}^{(k)} + \delta\mathbf{u}, \mathbf{m} + \delta\mathbf{m}; \mathbf{v}) = 0 \quad \forall \mathbf{v} \in \mathcal{V}_0 \tag{10}$$

$$\partial_{\mathbf{u}}F(\mathbf{u}^{(k)}, \mathbf{m}; \mathbf{v})[\delta_{\mathbf{m}}\mathbf{u}^{(k)}] + \partial_{\mathbf{m}}F(\mathbf{u}^{(k)}, \mathbf{m}; \mathbf{v})[\delta\mathbf{m}] = 0 \quad \forall \mathbf{v} \in \mathcal{V}_0 \tag{11}$$

$$D_{\mathbf{m}}\mathbf{u}^{(k)} = -[\partial_{\mathbf{u}}F^{(k)}]^{-1}\partial_{\mathbf{m}}F^{(k)}, \tag{12}$$

where $[\partial_{\mathbf{u}}F^{(k)}]^{-1}$ denotes the inverse of the tangent-stiffness $\partial_{\mathbf{u}}F^{(k)}$. However, the explicit computation of $D_{\mathbf{m}}\mathbf{u}^{(k)}$ can actually be avoided if we are only concerned with determining $D_{\mathbf{m}}\mathfrak{J}^{(k)}$:

$$D_{\mathbf{m}}\mathfrak{J}^{(k)} = \partial_{\mathbf{m}}\mathfrak{J}^{(k)} + [D_{\mathbf{m}}\mathbf{u}^{(k)}]^T \partial_{\mathbf{u}}\mathfrak{J}^{(k)} \tag{13}$$

$$D_{\mathbf{m}}\mathfrak{J}^{(k)} = \partial_{\mathbf{m}}\mathfrak{J}^{(k)} + [\partial_{\mathbf{m}}F^{(k)}]^T \left[-[\partial_{\mathbf{u}}F^{(k)}]^{-T}\partial_{\mathbf{u}}\mathfrak{J}^{(k)}\right] \tag{14}$$

$$D_{\mathbf{m}}\mathfrak{J}^{(k)} = \partial_{\mathbf{m}}\mathfrak{J}^{(k)} + [\partial_{\mathbf{m}}F^{(k)}]^T \mathbf{z}^{(k)} \tag{15}$$

where $\mathbf{z}^{(k)}$ is an intermediate solution vector (sometimes called the *adjoint* variable) which is determined by solving the problem implied in (14)

$$[\partial_{\mathbf{u}}F^{(k)}]^T \mathbf{z}^{(k)} = -\partial_{\mathbf{u}}\mathfrak{J}^{(k)} \tag{16}$$

In review, computing $D_{\mathbf{m}}\mathfrak{J}^{(k)}$ with the explicitly determined $D_{\mathbf{m}}\mathbf{u}^{(k)}$ requires as many linear solves as there are model parameters; on the other hand, computing $D_{\mathbf{m}}\mathfrak{J}^{(k)}$ directly always requires a single linear solve (since $\partial_{\mathbf{u}}\mathfrak{J}^{(k)}$ is a vector). Therefore, the second approach is preferred if $D_{\mathbf{m}}\mathbf{u}^{(k)}$ is not explicitly needed. By extension, the second order derivatives $D^2_{\mathbf{mm}}\mathfrak{J}^{(k)}$

can also be determined by leveraging the second approach. In this case, however, although computing the derivative $D^2_{\mathbf{mm}}\mathbf{u}^{(k)}$ can be avoided, computing $D_{\mathbf{m}}\mathbf{u}^{(k)}$ can not be. Finally, the Newton-Rhapson's algorithm can be used to update the model parameters $\mathbf{m}^{[n]}$ at the n'th iteration step as shown:

$$\Delta\mathbf{m}^{[n]} = -\left[D^2_{\mathbf{mm}}\mathfrak{J}^{[n]}\right]^{-1} D_{\mathbf{m}}\mathfrak{J}^{[n]} \tag{17}$$

In case a model parameter is required to be of a certain sign, the simple act of limiting the model parameter change is usually an adequate solution.

4. Model parameters sensitivity

The inverse problem of model parameter identification is a deterministic one. The solution is merely the best fit solution to the data that leads to the stationarity of the cost (6). Consequently, there are no additional outputs from the solution process such as a measure of the uncertainty in the inferred model parameters due to the uncertainties in the measurements. Therefore, it is useful to estimate the sensitivity of the model parameters with respect to the displacement field and pad reaction force measurements.

4.1. Deterministic evaluation

The model parameter sensitivities with respect $\mathbf{u}^{(k)}_{\text{msr}}$ and, similarly, with respect to $f^{(k)}_{\text{msr}}$ can be computed by solving a problem of this form

$$\delta_{\mathbf{v}} D_{\mathbf{m}}\mathfrak{J} = D^2_{\mathbf{mm}}\mathfrak{J}[\delta_{\mathbf{v}}\mathbf{m}] + \partial_{\mathbf{v}} D_{\mathbf{m}}\mathfrak{J}\,[\delta\mathbf{v}] = 0 \tag{18}$$

where $\mathbf{v}$ denotes a generic measurement and $\delta\mathbf{v}$ its directional change. Equation (18) says that the model cost should maintain its slope (e.g. of zero) by causing the model parameters to change accordingly based on a change in a measurement. For instance, substituting $\mathbf{v} \equiv \mathbf{u}^{(k)}_{\text{msr}}$ in (18) the solution to the model parameter sensitivity can be determined as

$$D_{\mathbf{u}^{(k)}_{\text{msr}}}\mathbf{m} = -\left[D^2_{\mathbf{mm}}\mathfrak{J}\right]^{-1} \partial_{\mathbf{u}^{(k)}_{\text{msr}}} D_{\mathbf{m}}\mathfrak{J}, \tag{19}$$

where $\partial_{\mathbf{u}^{(k)}_{\text{msr}}} D_{\mathbf{m}}\mathfrak{J}$ takes the form a rectangular matrix that has N_{m} rows and N_{dof} number of columns. Solely for the purpose of computing (19) we suppose that $\mathbf{u}_{\text{msr}}$ is discretized exactly like the displacement field $\mathbf{u}$, i.e. $\mathbf{u}_{\text{msr}} = \sum_{J=0}^{N_{\text{dof}}-1} \boldsymbol{\phi}_J\, \underline{u}_{\text{msr}\,J}$ where J is the DOF index, $\boldsymbol{\phi}$ is the N_{dim}-by-N_{dof}

matrix of the finite element nodal basis functions, and $\underline{\mathbf{u}}_{\mathrm{msr}}$ is the vector of DOFs. With this in mind, the entity $D_{u_{\mathrm{msr}}^{(k)}} m_{IJ}$ refers to the I'th model parameter's J'th sensitivity value with respect to the degree of freedom $\underline{u}_{\mathrm{msr}\,J}$.

In the case of the reaction force measurements, the J'th index in $D_{f_{\mathrm{msr}}^{(k)}} m_{IJ}$ generally refers to the reaction force component. In the extensometer experiment, however, the force is measured in just one direction; hence, $D_{f_{\mathrm{msr}}^{(k)}} m_{IJ}$ is effectively a vector where index J is unnecessary.

Equation (19) computes the model parameter sensitivities locally with respect to a measurement and boundary conditions at step k. In order to estimate the total change in the model parameters, all the local changes would need to be added up. This computation, however, is not straightforward because the measurement perturbations can be arbitrary. The model parameter sensitivity can be assessed more simply by considering the measurement variability in a statistical sense.

4.2. Statistical quantification

Assume the displacement field measurements can be characterized by the variance $\sigma^2_{u_{\mathrm{msr}}^{(k)}}$ that is spatially and temporally uncorrelated. The I'th model parameter variance $\sigma^2_{m_I|u_{\mathrm{msr}}^{(k)}}$ due to $\sigma^2_{u_{\mathrm{msr}}^{(k)}}$ can be estimated for step k as follows

$$\sigma^2_{m_I|u_{\mathrm{msr}}^{(k)}} = \mathrm{Var}\left(D_{u_{\mathrm{msr}}^{(k)}} m_{IJ}\, \delta u^{(k)}_{\mathrm{msr}\,J}\right) \tag{20}$$

$$\sigma^2_{m_I|u_{\mathrm{msr}}^{(k)}} = D_{u_{\mathrm{msr}}^{(k)}} m_{IJ}\, \mathrm{Cov}\left(\delta u^{(k)}_{\mathrm{msr}}\right)_{JK} D_{u_{\mathrm{msr}}^{(k)}} m_{IK} \tag{21}$$

$$\sigma^2_{m_I|u_{\mathrm{msr}}^{(k)}} = \sigma^2_{u_{\mathrm{msr}}^{(k)}} \sum_J \left(D_{u_{\mathrm{msr}}^{(k)}} m_{IJ}\right)^2 \tag{22}$$

The model parameter variance with respect to the reaction force measurement variance is obtained similarly

$$\sigma^2_{m_I|f_{\mathrm{msr}}^{(k)}} = \sigma^2_{f_{\mathrm{msr}}^{(k)}} \left(D_{f_{\mathrm{msr}}^{(k)}} m_I\right)^2 \tag{23}$$

In practice, it is more meaningful to report the sensitivity of a model parameter in terms of the relative standard deviation

$$\hat{\sigma}_{m_I|u_{\mathrm{msr}}^{(k)}} = \sigma_{m_I|u_{\mathrm{msr}}^{(k)}} \,/\, |m_I| \tag{24}$$

$$\hat{\sigma}_{m_I|f_{\mathrm{msr}}^{(k)}} = \sigma_{m_I|f_{\mathrm{msr}}^{(k)}} \,/\, |m_I| \tag{25}$$

The statistical quantification of the model parameter sensitivity is useful because the model parameter dependence on the measurements can be summarized simply. The results can give useful insight into how significant different measurements are on the model parameters.

4.3. Smoothing projection

We would like to visualize the model parameter sensitivity with respect to the displacement field measurements $\mathbf{u}_{\text{msr}}$ because the matrix $D_{\mathbf{u}^{(k)}_{\text{msr}}}\mathbf{m}$ is too abstract. To this end, each vector $D_{\mathbf{u}^{(k)}_{\text{msr}}} m_I$ can be transformed into a continuous vector function. The transformation problem is posed as follows. Suppose the sought sensitivity function is defined using the finite element basis functions as $\mathbf{g}_I = \sum_{K=0}^{N_{\text{dof}}-1} \boldsymbol{\phi}_K \underline{g}_{IK}$ where $\underline{\mathbf{g}}_I$ is the DOFs vector for the I'th model parameter sensitivity. Then, for any admissible perturbation in the displacement field measurements $\delta\mathbf{u}_{\text{msr}} = \sum_{J=0}^{N_{\text{dof}}-1} \boldsymbol{\phi}_J \delta\underline{u}_{\text{msr}\,J}$, require the model parameter change $\delta m_I = \sum_{J=0}^{N_{\text{dof}}} \delta\underline{u}_{\text{msr}\,J} D_{u^{(k)}_{\text{msr}}} m_{IJ}$ to be equivalently computable by the inner product of the functions $\delta\mathbf{u}_{\text{msr}}$ and $\mathbf{g}_I$:

$$\delta\underline{u}_{\text{msr}\,J} \int_{\Gamma_u} \boldsymbol{\phi}_J^T \boldsymbol{\phi}_K \underline{g}_{IK}\,\mathrm{d}x = \delta\underline{u}_{\text{msr}\,J} D_{u^{(k)}_{\text{msr}}} m_{IJ} \quad \forall \delta\underline{u}_{\text{msr}\,J} \tag{26}$$

The solution vector for the sensitivity function $\mathbf{g}_I$ is determined as

$$\underline{\mathbf{g}}_I = \mathbf{M}^{-1} D_{\mathbf{u}^{(k)}_{\text{msr}}} m_I \tag{27}$$

where $\mathbf{M} = \int_{\Gamma_u} \boldsymbol{\phi}^T \boldsymbol{\phi}\ \mathrm{d}x$ is the finite element mass-like matrix. Note that because the displacement field measurements are defined only on the subdomain Γ_u the sensitivity values outside this subdomain will be zero.

4.4. A prior estimate

The main drawback of (19) is that the model parameter sensitivity is defined only in the measurement subdomain. However, we would also like to have some idea of the significance of the displacement field measurements in the whole domain so that, for example, we could determine a more optimal subdomain for gathering displacement field measurements. Let us pretend we have displacement field measurements $\mathbf{u}^*_{\text{msr}}$ defined on the whole domain Ω. The fabricated cost $\mathfrak{J}^*_u$ due to the displacement field misfit is

$$\mathfrak{J}^*_u(\mathbf{m}) = \frac{1}{2} \int_{\Omega} (\mathbf{u}(\mathbf{m}) - \mathbf{u}^*_{\text{msr}})^2\ \mathrm{d}x \tag{28}$$

Let us suppose that the material model is very good such that the error between the measured and the model displacements is negligible, i.e. $\mathbf{u} \approx \mathbf{u}^*_{\text{msr}}$. In this case, the second derivative of $\mathfrak{J}^*_u$ with respect to the material model parameters $\mathbf{m}$ simplifies to the following:

$$D^2_{m_I m_J} \mathfrak{J}^*_u = \int_\Omega D_{m_I} u_i D_{m_J} u_i \, \mathrm{d}x + \int_\Omega (u_i - u^*_{\text{msr}i}) D^2_{m_I m_J} u_i \, \mathrm{d}x \tag{29}$$

$$D^2_{m_I m_J} \mathfrak{J}^*_u \approx \int_\Omega D_{m_I} u_i D_{m_J} u_i \, \mathrm{d}x \tag{30}$$

The second mixed derivative of $\mathfrak{J}^*_u$ with respect to $\mathbf{m}$ and $\mathbf{u}^*_{\text{msr}}$ reads

$$\partial_{\mathbf{u}^*_{\text{msr}}} D_{m_I} \mathfrak{J}^*_u [\delta \mathbf{u}^*_{\text{msr}}] = - \int_\Omega D_{m_I} u_i \, \delta u^*_{\text{msr}i} \, \mathrm{d}x \tag{31}$$

As a first attempt, one may try to compute the sensitivity $D_{\mathbf{u}^*_{\text{msr}}} \mathbf{m}$ as

$$D_{\mathbf{u}^*_{\text{msr}}} \mathbf{m} = \left(D^2_{\mathbf{mm}} \mathfrak{J}^*_u \right)^{-1} \left(-\partial_{\mathbf{u}^*_{\text{msr}}} D_{\mathbf{m}} \mathfrak{J}^*_u \right), \tag{32}$$

where $\partial_{\mathbf{u}^*_{\text{msr}}} D_{\mathbf{m}} \mathfrak{J}^*_u$ is a rectangular matrix that has N_{m} rows and N_{dof} number of columns corresponding to the DOFs of $\mathbf{u}^*_{\text{msr}}$. Unfortunately, it may not be generally possible to determine $D_{\mathbf{u}^*_{\text{msr}}} \mathbf{m}$ because $D^2_{\mathbf{mm}} \mathfrak{J}^*_u$ may not have an inverse. Nonetheless, the sensitivity can always be measured in an eigenvector direction. Suppose the non-zero eigenvalue and eigenvector are $\hat{\lambda}$ and $\hat{\mathbf{v}}$ respectively. Also suppose the displacement field measurements are discretized as $\mathbf{u}^*_{\text{msr}} = \sum_{J=0}^{N_{\text{dof}}-1} \boldsymbol{\phi}_J \underline{u}^*_{\text{msr}J}$ where J is the DOF index, $\boldsymbol{\phi}$ is matrix of finite element shape functions and $\underline{\mathbf{u}}^*_{\text{msr}}$ is the vector of DOFs. The model parameter change $\delta \hat{m}$ in the direction of $\hat{\mathbf{v}}$ can be computed as follows

$$\left(\hat{\mathbf{v}}^T D^2_{\mathbf{mm}} \mathfrak{J}^*_u \, \hat{\mathbf{v}} \right) \delta \hat{m} = \hat{\mathbf{v}}^T \int_\Omega D_{\mathbf{m}} u_i \, \delta u^*_{\text{msr}i} \, \mathrm{d}x \tag{33}$$

$$\delta \hat{m} = \left(\frac{\hat{v}_I}{\hat{\lambda}} \int_\Omega D_{m_I} u_i \; \phi_{iJ} \, \mathrm{d}x \right) \delta \underline{u}^*_{\text{msr}J} \tag{34}$$

Subsequently, the model parameter sensitivity can be defined as

$$D_{u^*_{\text{msr}}} \hat{m}_J = \frac{\hat{v}_I}{\hat{\lambda}} \int_\Omega D_{m_I} u_i \; \phi_{iJ} \, \mathrm{d}x \tag{35}$$

The vector $D_{\mathbf{u}^*_{\text{msr}}}\hat{m}$ of discrete sensitivities can be converted into a vector-valued function using the method described in Sec. 4.3. Suppose this function is defined as $\hat{\mathbf{g}} = \sum_{J=0}^{N_{\text{dof}}} \boldsymbol{\phi}_J \underline{\hat{g}}_J$. The DOFs vector $\underline{\hat{\mathbf{g}}}$ can be computed as

$$\underline{\hat{\mathbf{g}}} = \mathbf{M}^{-1}\, D_{\mathbf{u}^*_{\text{msr}}}\hat{m}, \tag{36}$$

where $\mathbf{M} = \int_\Omega \boldsymbol{\phi}^T \boldsymbol{\phi}\ \mathrm{d}x$ is the finite element mass matrix. The model parameter sensitivity function $\hat{\mathbf{g}}$, which is independent of the actual displacement field measurements and that is defined on the whole domain, can be used as an indicator for the most optimal displacement field measurement subdomain that has the most impact on the model parameters.

5. Implementation

The inverse solver and the sensitivity analysis routines are implemented in Python based on the finite element computational platform of FEniCS (Logg, 2007; Logg and Wells, 2010; Logg et al., 2012a). FEniCS is a collection of open-source libraries that enable highly automated solutions of differential equations. The FEniCS' Python interface called DOLFIN (Kirby and Logg, 2006; Logg and Wells, 2010; Logg et al., 2012c) provides an easy means to define finite element variational forms (Alnæs et al., 2014; Alnæs, 2012; Alnæs et al., 2012) that can then be translated (Kirby and Logg, 2006; Logg et al., 2012b) into low-level C++ finite element assembly code (Alnæs et al., 2009, 2012). Consequently, all the expensive finite element related computations can be handed over to the C++ runtime. Our implementation also heavily relies on the Python's popular scientific computing libraries, namely: scipy (Virtanen et al., 2020), numpy (van der Walt et al., 2011), matplotlib (Hunter, 2007), IPython (Pérez and Granger, 2007) and other parts of the toolstack (Oliphant, 2007; Millman and Aivazis, 2011). Our implementation, including the studied cases and other examples, is available at `https://github.com/danassutula/model_parameter_inference.git`.

6. Application

We consider a 2D hyperelastic model and plane-stress conditions. The effective load carrying thickness of the skin (and keloid) is assumed to be one millimeter. The computational domain is discretized using linear triangular finite elements in an unstructured mesh. The surface displacement field measurements, which are read-in in raw form as point-displacement values on a regular grid, are projected at the nodes of the underlying finite element mesh using a second degree least-squares meshless interpolation (Belytschko et al., 1996; Duarte and Oden, 1996; Nguyen et al., 2008).

6.1. Material model

Human skin is generally considered to be an anisotropic (Reihsner and Menzel, 1996; Meijer et al., 1999; Limbert, 2017) incompressible (Weiss et al., 1996; Nolan et al., 2014; Chagnon et al., 2015) material. In our case, however, fitting an anisotropic model would likely lead to an unreliable solution since all the measurements come from a uni-directional extension, i.e. there is no information along other load axes (Reihsner and Menzel, 1996; Groves et al., 2013; Boyer et al., 2013). On the other hand, (near-)incompressible material behavior is numerically burdensome since an additional incompressibility constraint and a new variable for the hydro-static stress must be involved (Lapeer et al., 2011; Nolan et al., 2014). As we consider a simple 2D plane-stress model, it makes little sense to choose an incompressible model over a compressible one given the added numerical complexity. Therefore, we assume the material model for both the healthy skin and the keloid to be a compressible hyperelastic Neo-Hookean material whose strain energy density is defined as shown

$$\Psi = C_1(I_1 - d - 2\ln\mathcal{J}) + D_1 \ln\mathcal{J}^2, \tag{37}$$

where C_1 and D_1 are the material model parameters and

$$I_1 = \operatorname{tr}\mathbf{C} \tag{38}$$

$$\mathcal{J} = \det\mathbf{F} \tag{39}$$

$$\mathbf{C} = \frac{1}{2}(\mathbf{F}^T\mathbf{F} - \mathbf{I}) \tag{40}$$

I_1 is the first invariant of the right Cauchy-Green deformation tensor $\mathbf{C}$, $\mathbf{F}$ is the deformation tensor whose components are $F_{ij} = \delta_{ij} + \partial u_i/\partial x_j$ where $i, j = 0, ..., d-1$, and d is the geometric dimension ($d = 2$). For consistency of (37) with linear-elasticity $C_1 = \mu/2$ and $D_1 = \lambda/2$ where λ is the Lamé's first parameter and μ is the shear modulus (Lamé's second parameter). It is useful to express μ and λ in terms of a pseudo Young's modulus E and pseudo Poisson's ratio ν as shown

$$\lambda = \frac{E\nu}{(1+\nu)\,(1-2\nu)} \tag{41}$$

$$\mu = \frac{E}{2(1+\nu)} \tag{42}$$

The advantage is that the material parameters are separated by physics; specifically, E carries units of pressure whereas ν is unitless. Besides this, the parameters are consistent with linear-elasticity.

6.2. Healthy skin model parameter identification

The model parameter identification is first carried out for the healthy skin. The extensometer devise is placed on the patient's arm without the keloid at an equivalent location as that of the keloid on the other arm. The rectangular computational domain is illustrated in Fig. 2. The square holes indicate the fixed pads of the extensometer. The boundaries of the holes have prescribed displacements: the left pad translates rigidly leftward relative to the right pad, which is fixed at zero displacement. The external boundaries are unrestrained. Fig. 2 highlights the displacement field measurement subdomain; it is roughly in the center between the two pads. This subdomain was chosen because the measurements could be acquired more reliably.

6.2.1. Measurements

The highlighted subdomain in Fig. 2 shows the location of the displacement field measurements. An example measurement, as shown in Fig. 3, consists of point-displacements on a regular grid. All displacements were computed relative to the in-plane position of the right pad. This was possible since the in-plane rigid translations and rotations of the extensometer had been tracked via landmarks assigned on the vertices of both pads. The reaction force *vs.* pad displacement measurements are shown in Fig. 4. The effective force-displacement relationship is taken to be the solid curve which is obtained by mean-filtering the measurements. The force-displacement relationship is defined up to a maximum displacement of 8 (mm). The hyperelastic behavior is largely exhibited from 6 (mm) of displacement.

6.2.2. Results

By virtue of the simplicity of the Neo-Hookean material model it was possible to fit the model parameters at each measurement step (i.e. the

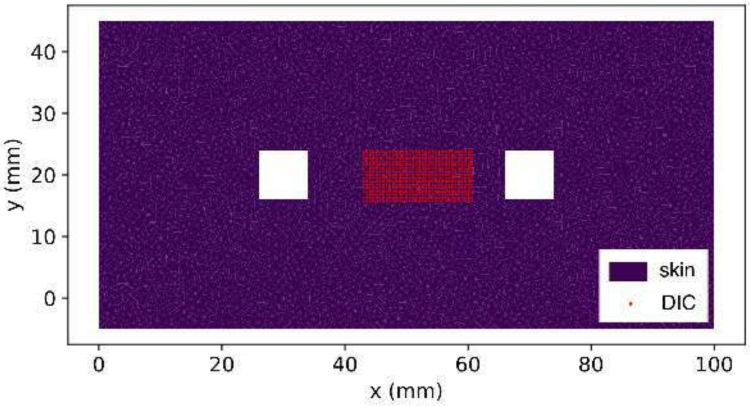

Figure 2: Computational domain of the healthy skin model. The highlighted grid of points indicates the displacement field measurements. The square holes represent the fixed pads.

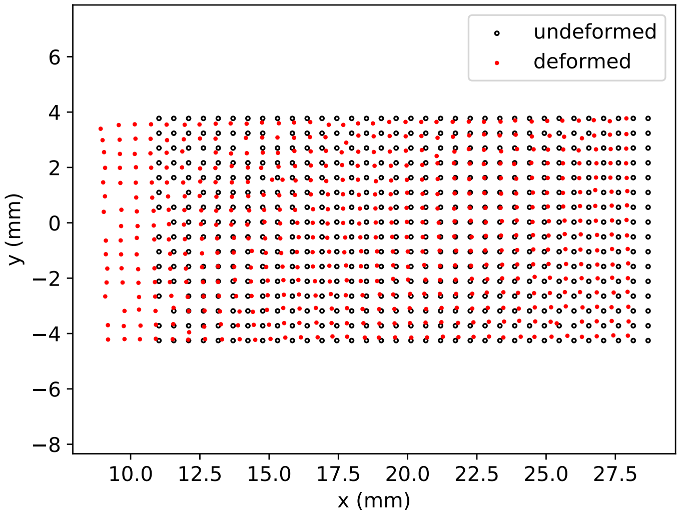

Figure 3: Displacement field measurements at the final measurement step for the healthy skin model parameter identification problem.

inverse problem (7)-(8) was solvable). The optimal model parameter values for each measurement step are shown in Fig. 5. The results show that the

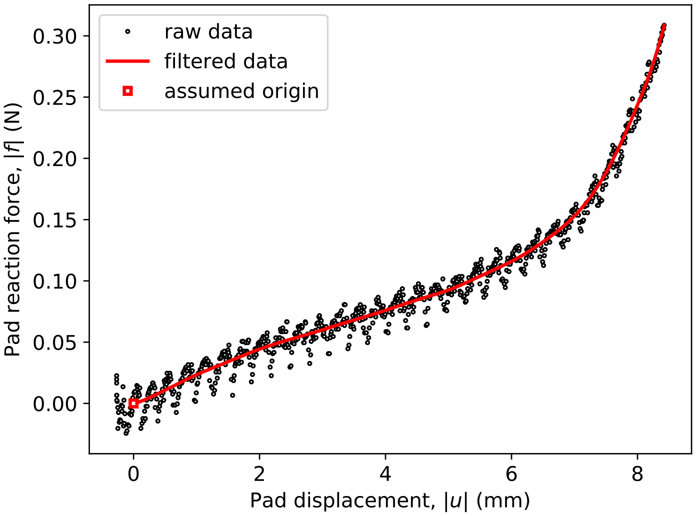

Figure 4: Pad reaction force *vs.* displacement measurements. The solid red curve, which was obtained by mean-filtering the data, represents the effective force-displacement load curve that was used in the healthy skin model parameter identification problem.

model parameter ν varies with each measurement. The inferred value steadily decreases from $\nu_{t=7} = 0.286$ to $\nu_{t=25} = 0.157$ with increasing load. On the other hand, the parameter E stays relatively constant at around $E = 0.028$ (N/mm^2). The model parameter dependence on measurements suggests that the choice of the model is not a very good one because the model parameter ν changes steadily with increasing load magnitude. Tab. 1 shows the obtained model parameter values when the model was fitted for all measurement steps.

Table 1: Inferred Neo-Hookean material parameters for the healthy skin model

E	0.028	N/mm^2
ν	0.195	[-]

The model parameter evolution with different finite element mesh sizes is shown in Fig.6. Although the convergence of the model parameters is not obvious at the finest finite element discretization (about 104k linear triangle elements), the values change sufficiently little for practical purposes.

The fitted Neo-Hookean model was able to match the measured reaction force well as shown by the results in Fig. 7. On the other hand, the dis-

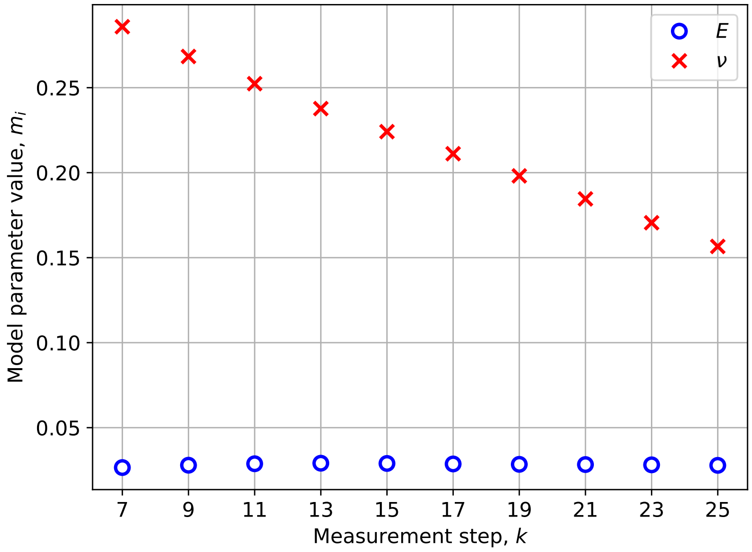

Figure 5: Healthy skin Neo-Hookean material parameters fitted at each measurement step.

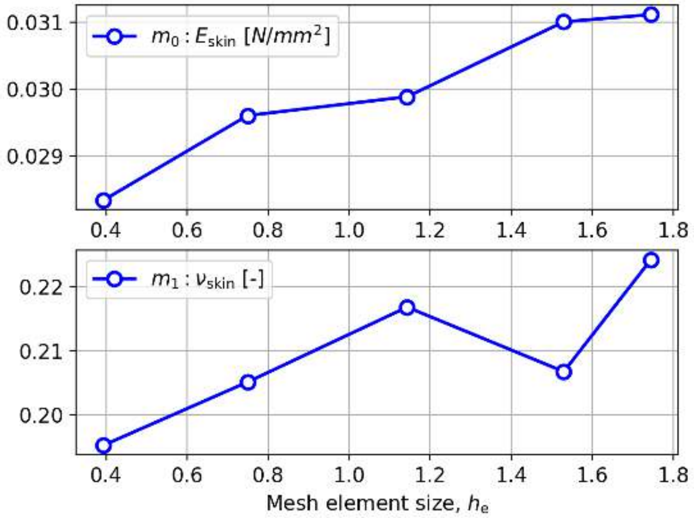

Figure 6: Healthy skin Neo-Hookean material model parameter value *vs.* mesh size.

placement field misfit turned out to be large. The error between the model displacement field and the measured displacement field is shown in Fig. 8.

The displacement misfit error is largest at the start of the load when the deformations are relatively small and decreases steadily with larger deformations (albeit the smallest error is still very large). The reason that the error is inversely correlated with the deformation magnitude can be attributed to the formulation of the displacement cost functional (3); specifically, the cost is biased towards larger deformations. For example, Fig. 9 shows that the model cost increases monotonically. An example displacement misfit error field at the final measurement step is shown in Fig. 10. The error vector field is principally in the direction of extension. Unfortunately, the Poisson's-like model parameter ν has very little to do with this type of deformation (it mainly affects the lateral deformation). Insofar as the total cost functional (6) is concerned, its derivatives are plotted in Fig. 11. The derivatives are zero on average over the measurement steps, which attests to the fact that the cost is minimized. Nevertheless, fitting the parameter ν is demonstrably hard. The parameter ν is depressed with respect to roughly the first half of the measurements and elevated with respect to the remaining half of the measurements. Even so, the parameter ν has little effect on the cost as implied by Fig. 10 since the error is principally in the direction of extension.

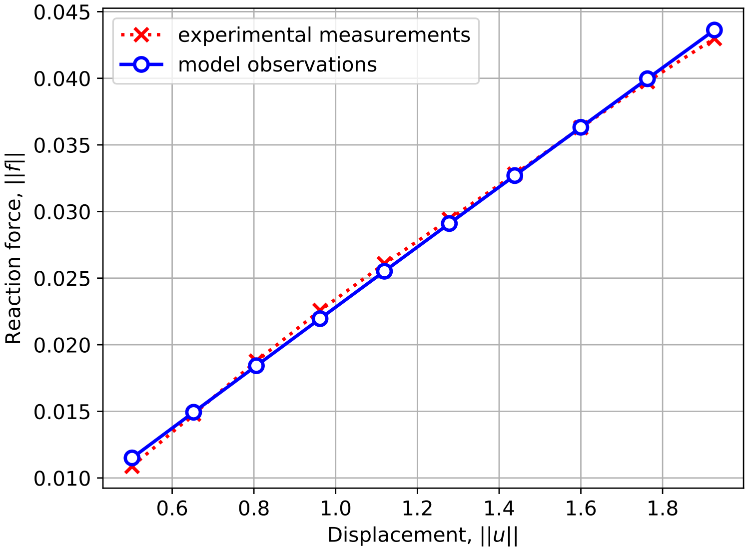

Figure 7: Model reaction force-displacement curve *vs.* measurements.

The model parameter sensitivities (refer to Sec. 4.1 for details) revealed

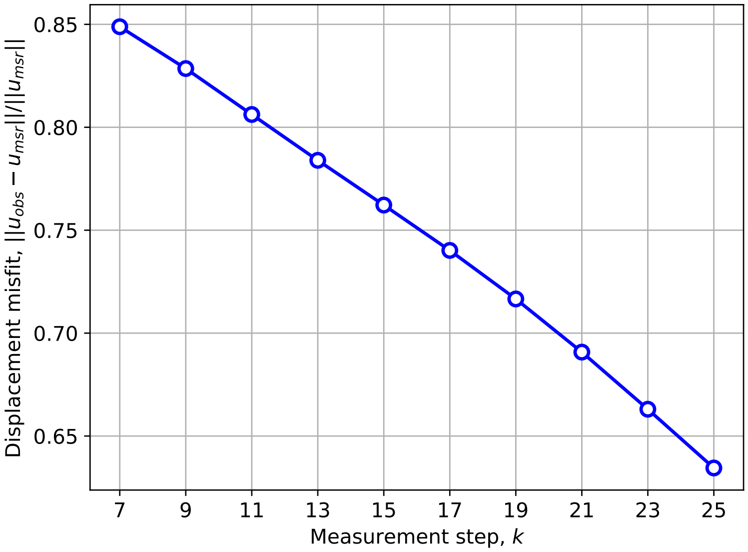

Figure 8: Error between the model and the measured displacements.

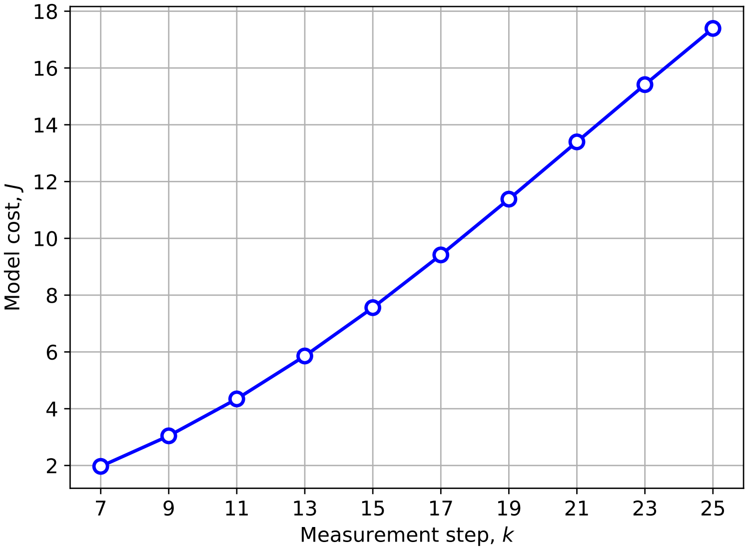

Figure 9: Cost of the healthy skin material model using the optimal material parameters.

that the parameter E was sensitive to the reaction force measurements and insensitive to the displacement field measurements. The opposite was ob-

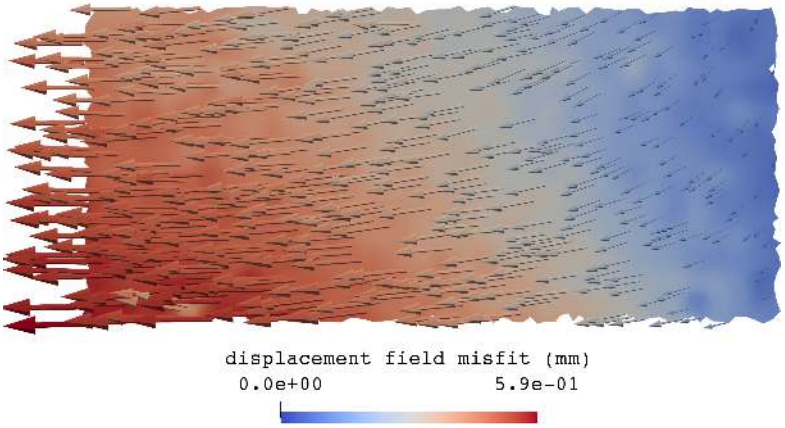

Figure 10: Displacement field misfit (i.e. $\mathbf{u} - \mathbf{u}_{\mathrm{msr}}$) for the final measurement step. (This plot is defined over the subdomain highlighted in Fig. 2.)

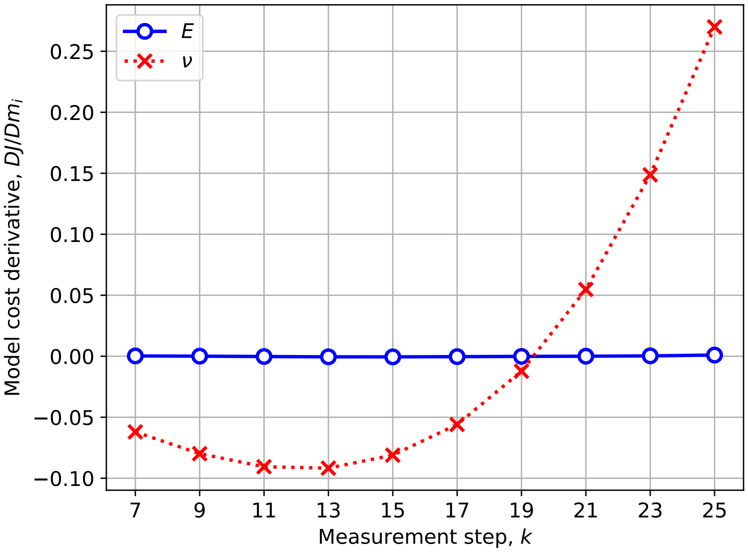

Figure 11: Cost derivatives with respect to model parameters of the healthy skin.

served regarding the sensitivity of the model parameter ν; it was found to be sensitive to the displacement field measurements and insensitive to the reaction force measurements. The sensitivities were quantified in terms of the relative standard deviation in the model parameters as caused by a unit standard deviation in the displacement field measurements (at the mesh nodes) and a unit standard deviation in the reaction force measurements; the results are shown in Fig. 12 and Fig. 13 respectively. More details about the sensitivity of parameter ν with respect to the displacement field measurements are revealed in Fig. 14. The vector field conveys the information that perturbing the displacement field measurements in the direction of this vector field will result in a positive change in the parameter ν. Note that ν is principally sensitive to the vertical component of the displacement field measurements, which is almost perpendicular to the displacement field error, as seen in Fig. 10.

An estimate of the model parameter ν sensitivity in the whole domain (refer to Sec. 4.4) is shown in Fig. 15. The reason that the intensity of the field is almost an order of magnitude smaller than that of the field shown in Fig. 14 is because of the difference in the domain size. Specifically, the average intensity of the sensitivity field for a bigger domain should be smaller.

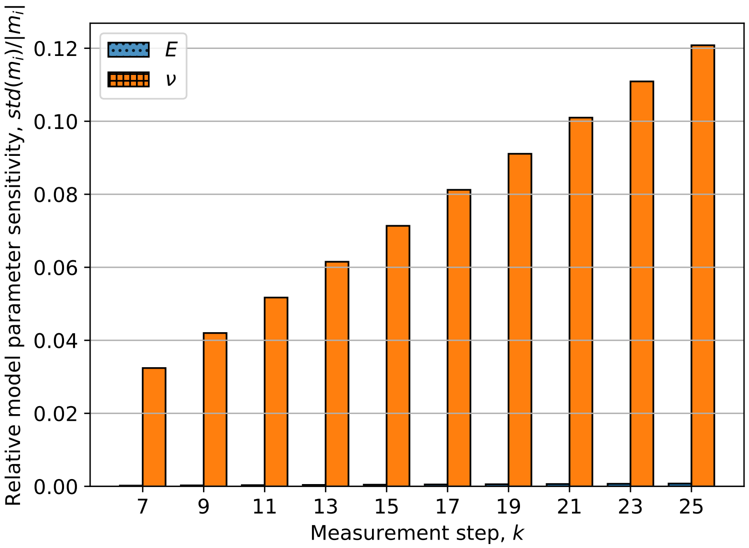

Figure 12: Healthy skin model parameter relative standard deviation assuming one standard deviation in the displacement field measurements at the mesh nodes.

6.3. Keloid scar model parameter identification

The model parameter identification for the keloid scar is performed considering the bi-material domain shown in Fig. 16. The Neo-Hookean material

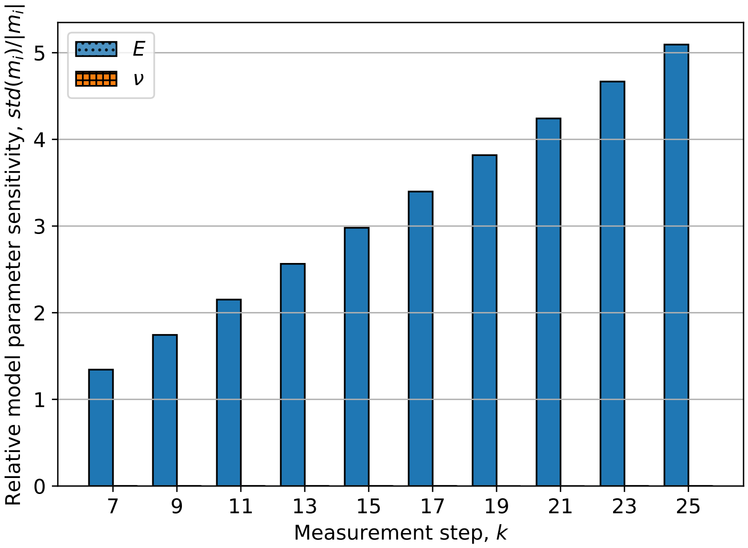

Figure 13: Healthy skin model parameter relative standard deviation assuming one standard deviation in the reaction force measurements.

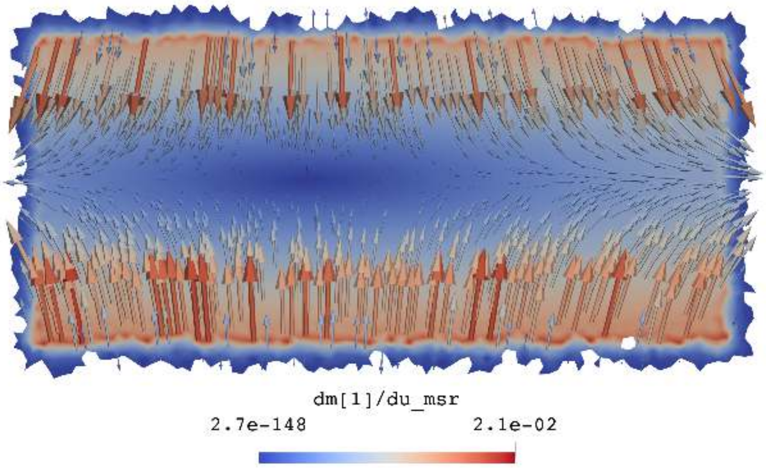

Figure 14: Model parameter ν sensitivity with respect to the displacement field measurements at the final measurement step. (This plot is defined over the subdomain highlighted in Fig. 2.)

model (refer to Sec. 6.1 for details) is assumed for each material subdomain. The model parameter values previously determined for the healthy skin were

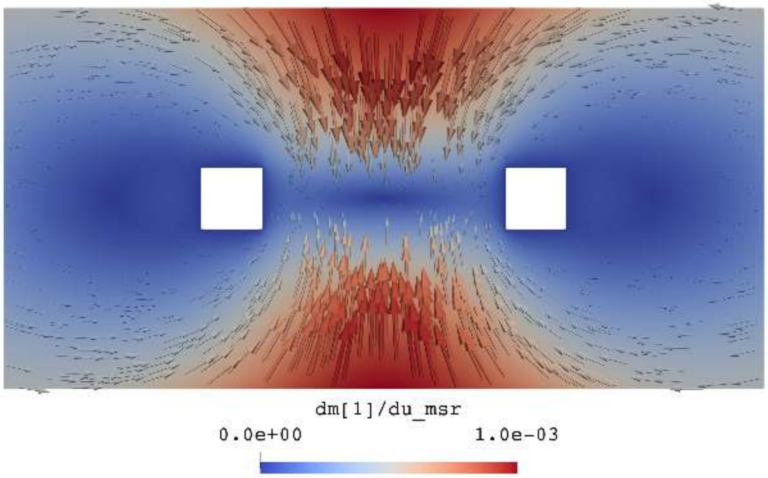

Figure 15: Model parameter ν estimated sensitivity with respect to displacement field measurements.

re-used for the healthy skin subdomain, namely $E_{\text{skin}} = 0.028$ (N/mm^2) and $\nu_{\text{skin}} = 0.195$. Therefore, only the keloid model parameters needed to be determined, specifically: E_{keloid} and ν_{keloid}.

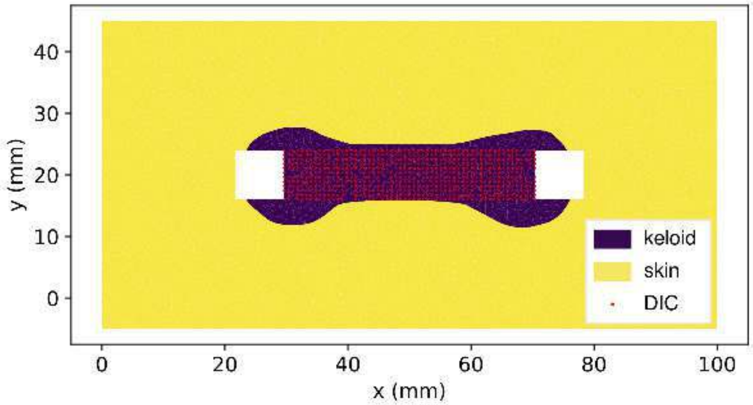

Figure 16: Bi-material skin-keloid model. The displacement field measurements are highlighted by the rectangular grid of points. The square holes represent the fixed pads.

6.3.1. *Measurements*

The highlighted subdomain in Fig. 16 shows the location of the displacement field measurement points. This subdomain was chosen because the displacement field measurements could be acquired more reliably. An example measurement of the point-displacements evaluated at the final measurement step is shown in Fig. 17. The measurements contained some spurious data points; consequently, these data were omitted from consideration. The measured reaction force *vs.* pad displacement relationship is shown in Fig. 18. The force is defined up to a displacement of roughly 4 (mm). The hyperelastic behavior is mainly observed from 2 (mm) of pad displacement. Since a Neo-Hookean material model can reproduce only a weakly nonlinear force-displacement relationship, the model parameter fitting was limited to a maximum pad displacement of 2 (mm).

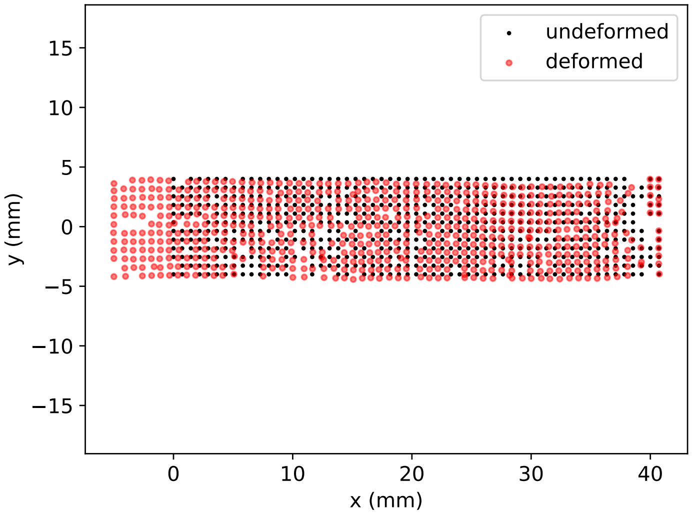

Figure 17: Displacement field measurements at the final measurement step for the keloid model parameter identification problem. (The point vacancies in the regular grid indicate spurious data that had to be discarded.)

6.3.2. *Results*

The model parameter evolution with mesh refinement is shown in Fig. 19. The finest resolution mesh consisted of 105k linear triangle elements. The convergence in the Young's modulus-like parameter E_{keloid} is fairly obvious. On the other hand, the Poisson's-like model parameter ν_{keloid} fails to con-

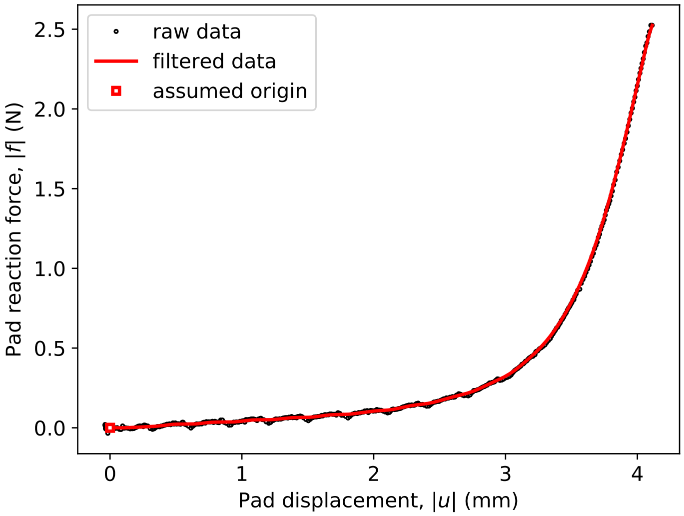

Figure 18: Pad reaction force *vs.* displacement measurements. The solid curve, which was obtained by mean-filtering the discrete data, represents the effective force-displacement load curve for the keloid model parameter identification problem.

verge. The presumed bi-material model parameters are given in Tab. 2. Fig. 20 shows that the bi-material model can match the measured force-displacement curve reasonably well. However, the displacement error, as shown by Fig. 21, is large – up to 14% for the last measurement step. Fig. 22 shows the distribution of this error in the measurement subdomain. The concentration of error likely arises due to the 3D shape of the keloid (above and within the skin) whose effects can not be accounted for by our simple 2D model. Another source of error is believed to be the 2D DIC technique that was used. In this case, a single camera is not so well suited for capturing the displacements on a curved surface of the skin. The measurements could have been more accurate if a stereoscopic camera system was used instead.

Table 2: Inferred Neo-Hookean material parameters for the skin-keloid bi-material model

E_{keloid}	0.077	N/mm^2
ν_{keloid}	0.35	[-]
E_{skin}	0.028	N/mm^2
ν_{skin}	0.195	[-]

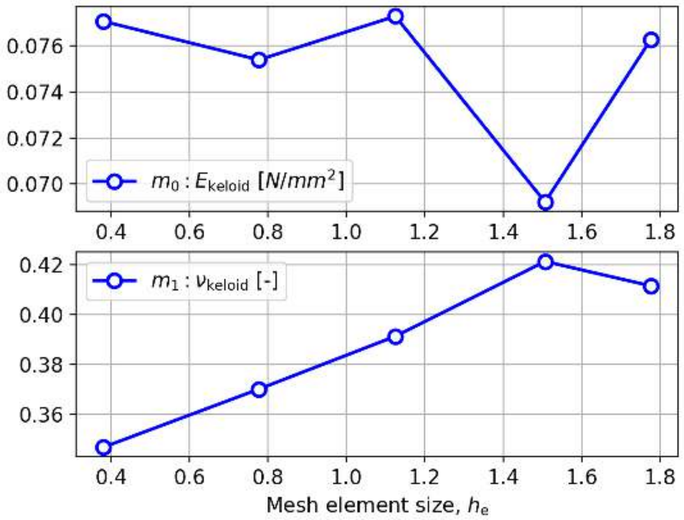

Figure 19: Keloid Neo-Hookean material model parameter values *vs.* mesh size.

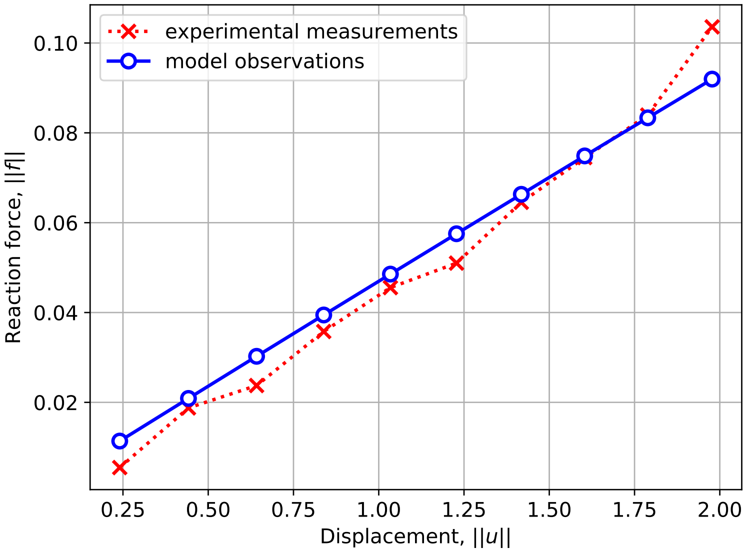

Figure 20: Bi-material model reaction force-displacement curve *vs.* measurements.

The keloid material model parameter sensitivities with respect to the displacement field measurements are given in Fig 23. The sensitivities with

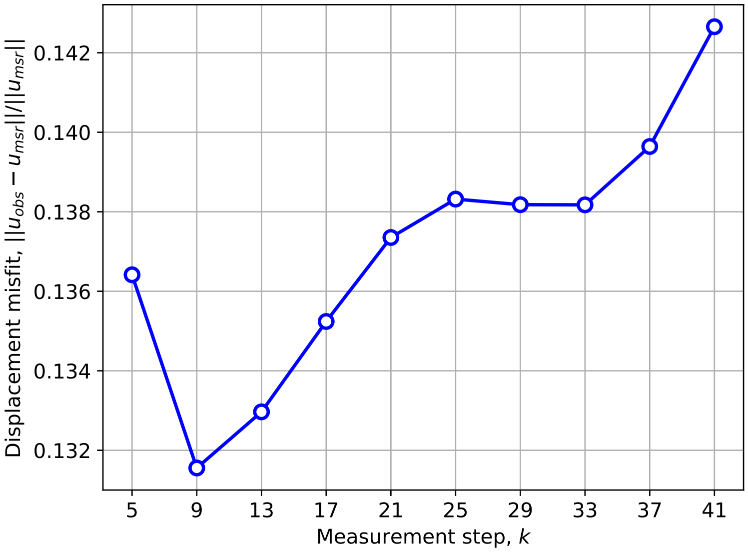

Figure 21: Error between the model and the measured displacements.

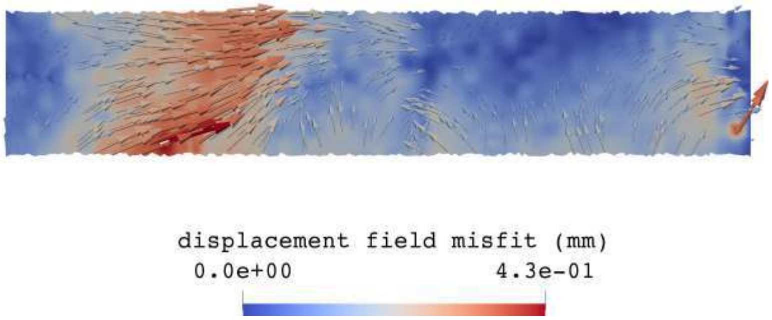

Figure 22: Displacement field misfit (i.e. $\mathbf{u} - \mathbf{u}_{\mathrm{msr}}$) for the final measurement step. (This plot is defined over the subdomain highlighted in Fig. 16.)

respect to the reaction force measurements are shown in Fig. 24. The parameter ν_{keloid} is mainly affected by the displacement field measurement whereas the reaction force measurements have a significant effect on both parameters (although the effect is much greater on parameter E_{keloid} than on ν_{keloid}). Fig 25 shows the sensitivity field for parameter ν_{keloid} with respect to the displacement field measurements in the measurement subdomain. An estimate of the sensitivity in the whole domain is shown in Fig. 26.

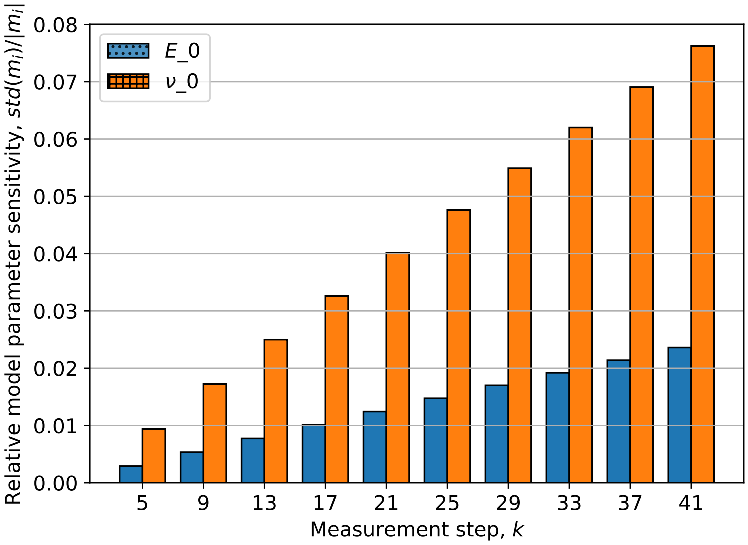

Figure 23: Keloid model parameter relative standard deviation assuming one standard deviation in the displacement field measurements at the mesh nodes.

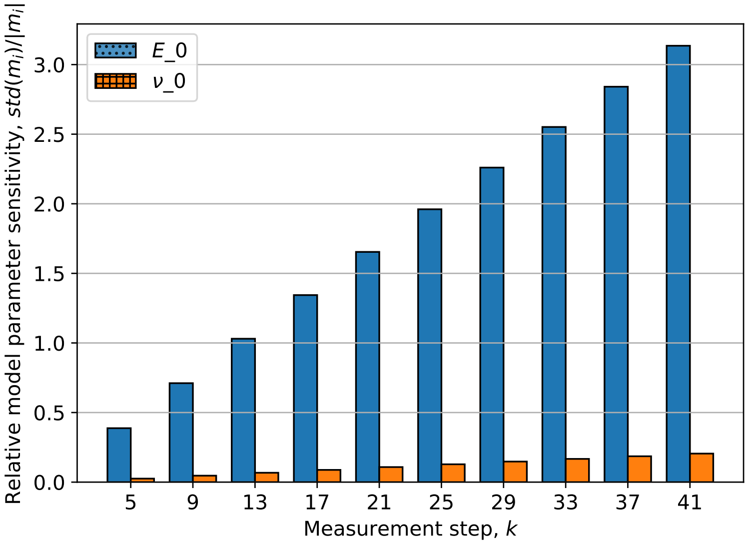

Figure 24: Keloid model parameter relative standard deviation assuming one standard deviation in the reaction force measurements.

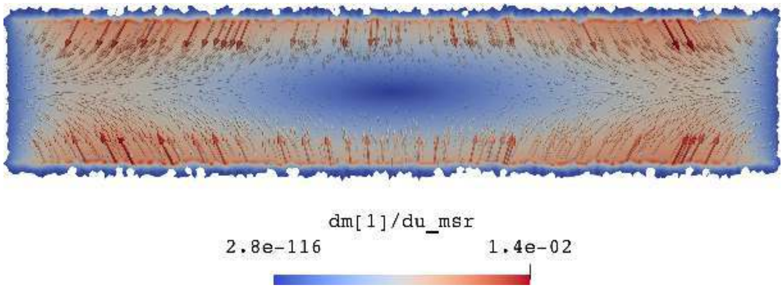

Figure 25: Model parameter ν_{keloid} sensitivity with respect to the displacement field measurements at the final measurement step. Note that the parameter is principally sensitive to the vertical component of the displacement field measurements. (This plot is defined over the subdomain highlighted in Fig. 2.)

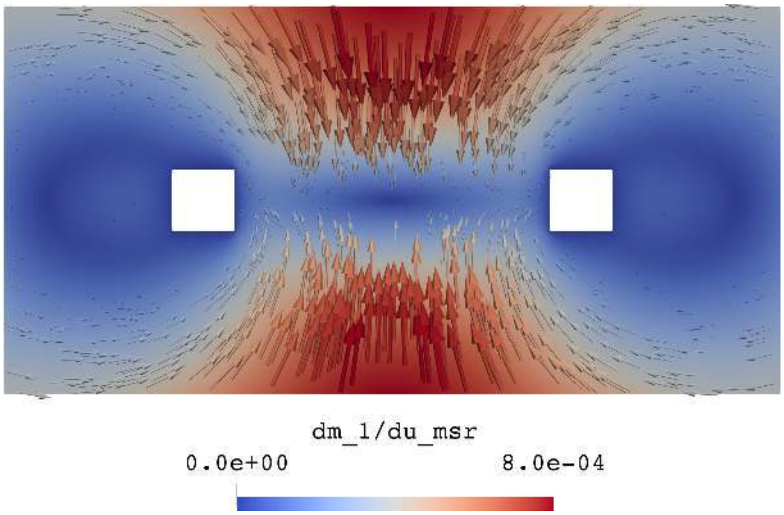

Figure 26: Model parameter ν_{keloid} estimated sensitivity with respect to displacement measurements.

7. Discussion and perspective

The idea behind the inverse method is quite simple: the aim is to minimize a cost functional that is a measure of the misfit between the model and the experiment. In practice, the inverse solution can be challenging since its success hinges on the experimental measurements being sufficiently rich to, in a sense, *activate* every model parameter. Although human skin is usually regarded as an incompressible, anisotropic and visco-elastic material, we considered in this study a much simpler model, namely, a compressible isotropic Neo-Hookean model. This decision was in part due to the already very strict 2D plane-stress modeling assumption and because the experimental measurements consisted only of uni-axial extensions, which lacked the information for fitting an anisotropic model. The present results indicate that the Neo-Hookean model, while capable of reproducing the almost-linear branch of the force-displacement relationship (e.g. Fig. 7 and 20), has significant displacement field misfit errors (e.g. Fig. 8 and 21). Although a more complex model may very well reduce these errors, there is the possibility of overfitting the 2D model. A similar work (Boyer et al., 2013) to ours assessed the mechanical properties of skin albeit on a forearm. In their case, a 2D orthotropic linear elastic plane-stress (also 1 mm thick) model was assumed. The results from 10 young female patients were the following. The minor value of the Young's modulus was $E_1 = 0.040 \pm 0.007$ (N/mm^2), the major value was $E_2 = 0.146 \pm 0.069$ (N/mm^2) and the Poisson's ratio was $\nu = 0.062 \pm 0.061$. Although these results can not be compared directly to ours, they are at least indicative of our findings: $E_{\text{skin}} = 0.028$ (N/mm^2) and $\nu_{\text{skin}} = 0.195$.

Accuracy of experimental measurements is of crucial importance for model parameter identification. Unfortunately, acquiring accurate measurements *in vivo* is a significant challenge and, consequently, measurement uncertainties are unavoidable. Therefore, when possible, it is important to quantify the model parameter uncertainties due to measurement uncertainties as part of an inverse solution. Addressing model uncertainties in biomechanics in general is of fundamental importance because of the severe variability between patients. This variability creates significant challenges for modeling and identifying which model parameters are the most important and which statistical distributions are best-suited to represent those parameters. The amount of cohort data is usually limited, although modern experimental methods enable the acquisition of multi-modal data which can enrich biological tissue models (Mascheroni and Schrefler, 2018). Once baseline information on a patient cohort is available, Bayesian updating can be used to develop a patient-specific understanding and to update the prior cohort-based knowledge (Hawkins-Daarud et al., 2013; Rappel et al., 2018, 2019, 2020). Subsequently, once parameter distributions are available, Monte Carlo simulations can be used to predict the impact of such parameters on quantities of interest to clinicians. Recent advances in this area show that, as expected, the relative importance of those biomechanical parameters depends on the set of boundary conditions applied upon the biomechanical system (Hauseux et al., 2018). Such approaches are also notoriously slow, which has led to the inception of accelerated methods such as derivative-based Monte Carlo (Hauseux et al., 2017). The next step in stochastic modeling of biological tissue is the design of experiments. Because experiments are costly and often invasive, it is critical to decrease the number of tests required to achieve a given level of understanding of the biomechanical system under consideration. The logical next steps for this work will be to develop a stochastic inverse method aimed at the identification of the sensitivity of parameters on boundary conditions and on other external factors, such as in (Barbone and Gokhale, 2004; Risholm et al., 2011; Hale et al., 2016). It is clear to the authors that the above represents a very large amount of work which is being largely undertaken by the community at large and requires the conjunct efforts from experimental to computational, through theoretical and statistical researchers. By working jointly, these three communities can make significant progress in the design of new experimental devices, new *in silico* experiments, new phantom materials, and in devising digital twins to better understand human biological tissues (Bordas et al., 2018; Ley and Bordas, 2018).

8. Summary

The paper focused on the problem of hyperelastic model parameter identification and model parameter sensitivity analysis for a keloid scar and healthy skin. The patient specific experimental measurements were acquired *in vivo* using a custom-made uni-axial extensometer. A two-parameter Neo-Hookean material model was assumed for both the keloid and the healthy skin. The model parameter identification was carried out in two separate analysis. The model parameters were first identified for the healthy skin. Then, using the healthy skin parameters in the skin-keloid bi-material model, the keloid material parameters were determined. The fitted models could reproduce the measured reaction forces well. On the other hand, the displacement field misfit errors were significant. The healthy skin model displacements were more than 65% off from measurements, whereas the skin-keloid bi-material model displacements were up to 14% off. It is understood that the unquantified errors the displacement field measurements from the DIC analysis play a part in the current results. On the other hand, the sensitivity analysis could also explain the large errors. Specifically, the parameter governing the model's kinematic field turned out to be insensitive to displacement measurements in the direction of the observed error. In essence, the model's displacement misfit error would be large no matter the value of the model parameter. Finally, we proposed a simple way to estimate the model parameter sensitivity with respect to the surface displacement field measurements in the whole domain. The estimate depends only on the boundary conditions and on the assumed model parameter values and is otherwise independent of the actual surface displacement field measurements. This information can aid in the design of experiments, specifically in localizing the optimal displacement field measurement sites for the maximum impact on model parameters.

Acknowledgments

The authors acknowledge the financial support of Region de Bourgogne Franche-Comté, France (grants n° 2017-Y-06397, n° 2018-Y-04536, n° 2019-Y-10541). P. Hauseux acknowledges the support of the Fonds National de la Recherche Luxembourg FNR (grant n° O17-QCCAAS-11758809). S. Bordas thanks the FEMTO-ST Institute, Department of Applied Mechanics, and the Laboratoire de Mathématiques de Besançon for their fellowship opportunities, and also acknowledges the discussions with Dr. Olga Barrera, Oxford University. D. Baroli acknowledges the support of FEDER funding innovation and DFG Clusters of Excellence: Internet of Production. M. Sensale thanks the University of Luxembourg, Institute of Computational Engineering for the visiting fellowship opportunity.

References

Abdel-Fattah, A.M.A., 1976. The evolution of pre-sternal keloids. British Journal of Plastic Surgery 29, 56–58.

Akaishi, S., Akimoto, M., Ogawa, R., Hyakusoku, H., 2008. The Relationship Between Keloid Growth Pattern and Stretching Tension. Annals of Plastic Surgery 60, 445–451.

Alnæs, M.S., 2012. UFL: a finite element form language, in: Logg, A., Mardal, K.A., Wells, G.N. (Eds.), Automated Solution of Differential Equations by the Finite Element Method. Springer. volume 84 of *Lecture Notes in Computational Science and Engineering*. chapter 17, pp. 303–338.

Alnæs, M.S., Logg, A., Mardal, K.A., 2012. UFC: a finite element code generation interface, in: Logg, A., Mardal, K.A., Wells, G.N. (Eds.), Automated Solution of Differential Equations by the Finite Element Method.

Springer. volume 84 of *Lecture Notes in Computational Science and Engineering*. chapter 16, pp. 283–302.

Alnæs, M.S., Logg, A., Mardal, K.A., Skavhaug, O., Langtangen, H.P., 2009. Unified framework for finite element assembly. International Journal of Computational Science and Engineering 4, 231–244.

Alnæs, M.S., Logg, A., Ølgaard, K.B., Rognes, M.E., Wells, G.N., 2014. Unified Form Language: A domain-specific language for weak formulations of partial differential equations. ACM Transactions on Mathematical Software 40, 1–37.

Alotta, G., Barrera, O., Cocks, A.C.F., Paola, M.D., 2017. On the behavior of a three-dimensional fractional viscoelastic constitutive model. Meccanica 52, 2127–2142.

Alotta, G., Barrera, O., Pegg, E.C., 2018. Viscoelastic material models for more accurate polyethylene wear estimation. The Journal of Strain Analysis for Engineering Design 53, 302–312.

Annaidh, A.N., Bruyère, K., Destrade, M., Gilchrist, M.D., Otténio, M., 2012. Characterization of the anisotropic mechanical properties of excised human skin. Journal of the Mechanical Behavior of Biomedical Materials 5, 139–148.

Avril, S., Bonnet, M., Bretelle, A.S., Grédiac, M., Hild, F., Ienny, P., Latourte, F., Lemosse, D., Pagano, S., Pagnacco, E., Pierron, F., 2008. Overview of identification methods of mechanical parameters based on full-field measurements. Experimental Mechanics 48, 381–402.

Bahreman, M., Darijani, H., Fooladi, M., 2015. Constitutive modeling of isotropic hyperelastic materials using proposed phenomenological models in terms of strain invariants. Polymer Engineering & Science 56, 299–308.

Barbone, P.E., Gokhale, N.H., 2004. Elastic modulus imaging: on the uniqueness and nonuniqueness of the elastography inverse problem in two dimensions. Inverse Problems 20, 283–296.

Barrera, O., Bologna, E., Zingales, M., Alotta, G., 2018. Experimental characterization of the human meniscal tissue, in: 2018 IEEE 4th International Forum on Research and Technology for Society and Industry (RTSI), IEEE. pp. 1–5.

Belytschko, T., Krongauz, Y., Organ, D., Fleming, M., Krysl, P., 1996. Meshless Methods: An Overview and Recent Developments. Computer Method in Applied Mechanics and Engineering 139, 3–47.

Bordas, S.P.A., Natarajan, S., Zilian, A., 2018. Mathematical modelling and artificial intelligence in luxembourg: Twenty PhD students to be trained in data-driven modelling. ERCIM News 115, 39–40.

Boyer, G., Molimard, J., Ben Tkaya, M., Zahouani, H., Pericoi, M., Avril, S., 2013. Assessment of the in-plane biomechanical properties of human skin using a finite element model updating approach combined with an optical full-field measurement on a new tensile device. Journal of the Mechanical Behavior of Biomedical Materials 27, 273–282.

Chagnon, G., Rebouah, M., Favier, D., 2015. Hyperelastic energy densities for soft biological tissues: A review. Journal of Elasticity 120, 129–160.

Chambert, J., Lihoreau, T., Joly, S., Chatelain, B., Sandoz, P., Humbert, P., Jacquet, E., Rolin, G., 2019. Multimodal investigation of a keloid scar by combining mechanical tests in vivo with diverse imaging techniques. Journal of the Mechanical Behavior of Biomedical Materials 99, 206–215.

Cowin, S.C. (Ed.), 2001. Bone Mechanics Handbook. 2nd ed., CRC Press, Boca Raton.

Diridollou, S., Berson, M., Vabre, V., Black, D., Karlsson, B., Auriol, F., Gregoire, J.M., Yvon, C., Vaillant, L., Gall, Y., Patat, F., 1998. An in vivo method for measuring the mechanical properties of the skin using ultrasound. Ultrasound in Medicine & Biology 24, 215–224.

Duarte, C.A., Oden, J.T., 1996. H-p clouds—an h-p meshless method. Numerical Methods for Partial Differential Equations 12, 673–705.

Evans, S.L., Holt, C.A., 2009. Measuring the mechanical properties of human skin in vivo using digital image correlation and finite element modelling. The Journal of Strain Analysis for Engineering Design 44, 337–345.

Finlay, B., 1970. Dynamic mechanical testing of human skin ‘in vivo’. Journal of Biomechanics 3, 557–568.

Fthenakis, C.G., Maes, D.H., Smith, W.P., 1991. In vivo assessment of skin elasticity using ballistometry. Journal of the Society of Cosmetic Chemists 42, 211–222.

Fung, Y.C., 1993. Biomechanics: Mechanical Properties of Living Tissues. 2nd ed., Springer-Verlag, New York.

Groves, R.B., Coulman, S.A., Birchall, J.C., Evans, S.L., 2013. An anisotropic, hyperelastic model for skin: Experimental measurements, finite element modelling and identification of parameters for human and murine skin. Journal of the Mechanical Behavior of Biomedical Materials 18, 167–180.

Hale, J.S., Farrell, P.E., Bordas, S.P.A., 2016. Elastography under uncertainty, in: Computational Sciences for Medicine Modelling and Simulation for Surgery, University of Luxembourg. December, 12–15.

Halim, A.S., Emami, A., Salahshourifar, I., Kannan, T.P., 2012. Keloid scarring: understanding the genetic basis, advances, and prospects. Archives of Plastic Surgery 39, 184–189.

Hatze, H., 1974. The meaning of the term 'biomechanics'. Journal of Biomechanics 7, 189–190.

Hauseux, P., Hale, J.S., Bordas, S.P.A., 2017. Accelerating Monte Carlo estimation with derivatives of high-level finite element models. Computer Methods in Applied Mechanics and Engineering 318, 917–936.

Hauseux, P., Hale, J.S., Cotin, S., Bordas, S.P.A., 2018. Quantifying the uncertainty in a hyperelastic soft tissue model with stochastic parameters. Applied Mathematical Modelling 62, 86–102.

Hawkins-Daarud, A., Prudhomme, S., van der Zee, K.G., Oden, J.T., 2013. Bayesian calibration, validation, and uncertainty quantification of diffuse interface models of tumor growth. Journal of Mathematical Biology 67, 1457–1485.

Hunter, J.D., 2007. Matplotlib: a 2D graphics environment. Computing in Science & Engineering 9, 90–95.

Jacquet, E., Chambert, J., Pauchot, J., Sandoz, P., 2017a. Intra- and inter-individual variability in the mechanical properties of the human skin from in vivo measurements on 20 volunteers. Skin Research and Technology 23, 491–499.

Jacquet, E., Joly, S., Chambert, J., Rekik, K., Sandoz, P., 2017b. Ultra-light extensometer for the assessment of the mechanical properties of the human skin in vivo. Skin Research and Technology 23, 531–538.

Kim, W.J.H., Levinson, H., Gittes, G.K., Longaker, M.T., 2000. Molecular mechanisms in keloid biology, in: Rodrigues, A.D. (Ed.), Scarless wound healing. CRC Press, Boca Raton, pp. 172–182.

Kirby, R.C., Logg, A., 2006. A compiler for variational forms. ACM Transactions on Mathematical Software 32, 417–444.

Laiacona, D., Cohen, J.M., Coulon, K., Lipsky, Z.W., Maiorana, C., Boltyanskiy, R., Dufresne, E.R., German, G.K., 2019. Non-invasive in vivo quantification of human skin tension lines. Acta Biomaterialia 88, 141–148.

Lapeer, R.J., Gasson, P.D., Karri, V., 2011. A Hyperelastic Finite-Element Model of Human Skin for Interactive Real-Time Surgical Simulation. IEEE Transactions on Biomedical Engineering 58, 1013–1022.

Ley, C., Bordas, S.P.A., 2018. What makes data science different? a discussion involving statistics2.0 and computational sciences. International Journal of Data Science and Analytics 6, 167–175.

Limbert, G., 2017. Mathematical and computational modelling of skin biophysics: a review. Proceedings of the Royal Society A: Mathematical, Physical and Engineering Sciences 473, 20170257.

Logg, A., 2007. Automating the Finite Element Method. Archives of Computational Methods in Engineering 14, 93–138.

Logg, A., Mardal, K.A., Wells, G.N. (Eds.), 2012a. Automated Solution of Differential Equations by the Finite Element Method: The FEniCS Book. volume 84 of *Lecture Notes in Computational Science and Engineering*. Springer, Berlin Heidelberg.

Logg, A., Ølgaard, K.B., Rognes, M.E., Wells, G.N., 2012b. FFC: the FEniCS form compiler, in: Logg, A., Mardal, K.A., Wells, G.N. (Eds.), Automated Solution of Differential Equations by the Finite Element Method. Springer. volume 84 of *Lecture Notes in Computational Science and Engineering*. chapter 11, pp. 227–238.

Logg, A., Wells, G.N., 2010. DOLFIN: Automated finite element computing. ACM Transactions on Mathematical Software 37, 20:1–20:28.

Logg, A., Wells, G.N., Hake, J., 2012c. DOLFIN: a C++/Python finite element library, in: Logg, A., Mardal, K.A., Wells, G.N. (Eds.), Automated Solution of Differential Equations by the Finite Element Method. Springer. volume 84 of *Lecture Notes in Computational Science and Engineering*. chapter 10, pp. 173–225.

Maiti, R., Gerhardt, L.C., Lee, Z.S., Byers, R.A., Woods, D., Sanz-Herrera, J.A., Franklin, S.E., Lewis, R., Matcher, S.J., Carré, M.J., 2016. In vivo measurement of skin surface strain and sub-surface layer deformation induced by natural tissue stretching. Journal of the Mechanical Behavior of Biomedical Materials 62, 556–569.

Mascheroni, P., Schrefler, B.A., 2018. In Silico Models for Nanomedicine: Recent Developments. Current Medicinal Chemistry 25, 4192–4207.

Meijer, R., Douven, L.F.A., Oomens, C.W.J., 1999. Characterisation of anisotropic and non-linear behaviour of human skin in vivo. Computer Methods in Biomechanics and Biomedical Engineering 2, 13–27.

Millman, K.J., Aivazis, M., 2011. Python for scientists and engineers. Computing in Science & Engineering 13, 9–12.

Müller, B., Elrod, J., Pensalfini, M., Hopf, R., Distler, O., Schiestl, C., Mazza, E., 2018. A novel ultra-light suction device for mechanical characterization of skin. PloS One 13, e0201440.

Nagasao, T., Aramaki-Hattori, N., Shimizu, Y., Yoshitatsu, S., Takano, N., Kishi, K., 2013. Transformation of keloids is determined by stress occurrence patterns on peri-keloid regions in response to body movement. Medical Hypotheses 81, 136–141.

Nguyen, V.P., Rabczuk, T., Bordas, S.P.A., Duflot, M., 2008. Meshless methods: A review and computer implementation aspects. Mathematics and Computers in Simulation 79, 763–813. arXiv:10.1.1.160.1721.

Niklas, K.J., 1992. Plant biomechanics: an engineering approach to plant form and function. University of Chicago press.

Nolan, D.R., Gower, A.L., Destrade, M., Ogden, R.W., McGarry, J.P., 2014. A robust anisotropic hyperelastic formulation for the modelling of soft tissue. Journal of the Mechanical Behavior of Biomedical Materials 39, 48–60.

Ogawa, R., 2008. Keloid and hypertrophic scarring may result from a mechanoreceptor or mechanosensitive nociceptor disorder. Medical Hypotheses 71, 493–500.

Ogawa, R., Okai, K., Tokumura, F., Mori, K., Ohmori, Y., Huang, C., Hyakusoku, H., Akaishi, S., 2012. The relationship between skin stretching/contraction and pathologic scarring: The important role of mechanical forces in keloid generation. Wound Repair and Regeneration 20, 149–157.

Ogden, R.W., 1972. Large deformation isotropic elasticity: on the correlation of theory and experiment for compressible rubberlike solids. Proceedings of the Royal Society of London. A. Mathematical and Physical Sciences 328, 567–583.

Oliphant, T.E., 2007. Python for scientific computing. Computing in Science & Engineering 9, 10–20.

Ottenio, M., Tran, D., Annaidh, A.N., Gilchrist, M.D., Bruyère, K., 2015. Strain rate and anisotropy effects on the tensile failure characteristics of human skin. Journal of the Mechanical Behavior of Biomedical Materials 41, 241–250.

Pailler-Mattei, C., Bec, S., Zahouani, H., 2008. In vivo measurements of the elastic mechanical properties of human skin by indentation tests. Medical Engineering & Physics 30, 599–606.

Pan, S., Malhotra, D., Germann, N., 2019. Nonlinear viscoelastic properties of native male human skin and in vitro 3D reconstructed skin models under

LAOS stress. Journal of the Mechanical Behavior of Biomedical Materials 96, 310–323.

Pence, T.J., Gou, K., 2015. On compressible versions of the incompressible neo-Hookean material. Mathematics and Mechanics of Solids 20, 157–182.

Pérez, F., Granger, B.E., 2007. IPython: a system for interactive scientific computing. Computing in Science & Engineering 9, 21–29.

Rappel, H., Beex, L.A.A., Bordas, S.P.A., 2018. Bayesian inference to identify parameters in viscoelasticity. Mechanics of Time-Dependent Materials 22, 221–258.

Rappel, H., Beex, L.A.A., Hale, J.S., Noels, L., Bordas, S.P.A., 2020. A tutorial on bayesian inference to identify material parameters in solid mechanics. Archives of Computational Methods in Engineering 27, 361–385.

Rappel, H., Beex, L.A.A., Noels, L., Bordas, S.P.A., 2019. Identifying elastoplastic parameters with Bayes' theorem considering output error, input error and model uncertainty. Probabilistic Engineering Mechanics 55, 28–41.

Rashid, B., Destrade, M., Gilchrist, M.D., 2014. Mechanical characterization of brain tissue in tension at dynamic strain rates. Journal of the Mechanical Behavior of Biomedical Materials 33, 43–54.

Reihsner, R., Menzel, E.J., 1996. On the orthogonal anisotropy of human skin as a function of anatomical region. Connective Tissue Research 34, 145–160.

Risholm, P., Ross, J., Washko, G.R., Wells, W.M., 2011. Probabilistic elastography: estimating lung elasticity, in: Biennial International Conference on Information Processing in Medical Imaging, Springer. pp. 699–710.

Rivlin, R.S., 1948. Large elastic deformations of isotropic materials iv. further developments of the general theory. Philosophical Transactions of the Royal Society of London. Series A, Mathematical and Physical Sciences 241, 379–397.

Robles, D.T., Berg, D., 2007. Abnormal wound healing: keloids. Clinics in Dermatology 25, 26–32.

Screen, H.R.C., 2008. Investigating load relaxation mechanics in tendon. Journal of the Mechanical Behavior of Biomedical Materials 1, 51–58.

Sutton, M., Yan, J., Tiwari, V., Schreier, H., Orteu, J., 2008. The effect of out-of-plane motion on 2D and 3D digital image correlation measurements. Optics and Lasers in Engineering 46, 746–757.

Tonge, T.K., Atlan, L.S., Voo, L.M., Nguyen, T.D., 2013. Full-field bulge test for planar anisotropic tissues: Part I–Experimental methods applied to human skin tissue. Acta Biomaterialia 9, 5913–5925.

Van Dommelen, J.A.W., Van der Sande, T.P.J., Hrapko, M., Peters, G.W.M., 2010. Mechanical properties of brain tissue by indentation: interregional variation. Journal of the Mechanical Behavior of Biomedical Materials 3, 158–166.

Virtanen, P., Gommers, R., Oliphant, T.E., Haberland, M., Reddy, T., Cournapeau, D., Burovski, E., Peterson, P., Weckesser, W., Bright, J., et al., 2020. SciPy 1.0: fundamental algorithms for scientific computing in Python. Nature Methods 17, 261–272.

van der Walt, S., Colbert, S.C., Varoquaux, G., 2011. The NumPy array: a structure for efficient numerical computation. Computing in Science & Engineering 13, 22–30.

Wan Abas, W.A.B., 1994. Biaxial tension test of human skin in vivo. Biomedical Materials and Engineering 4, 473–486.

Wan Abas, W.A.B., Barbenel, J.C., 1982. Uniaxial tension test of human skin in vivo. Journal of Biomedical Engineering 4, 65–71.

Weiss, J.A., Maker, B.N., Govindjee, S., 1996. Finite element implementation of incompressible, transversely isotropic hyperelasticity. Computer Methods in Applied Mechanics and Engineering 135, 107–128.

Wex, C., Arndt, S., Stoll, A., Bruns, C., Kupriyanova, Y., 2015. Isotropic incompressible hyperelastic models for modelling the mechanical behaviour of biological tissues: a review. Biomedical Engineering / Biomedizinische Technik 60, 577—592.

Yeoh, O.H., 1993. Some forms of the strain energy function for rubber. Rubber Chemistry and Technology 66, 754–771.

Zhang, X., Greenleaf, J.F., 2007. Estimation of tissue's elasticity with surface wave speed. The Journal of the Acoustical Society of America 122, 2522–2525.